RESEARCH ARTICLE | DECEMBER 22 2025

# Peeling-ballooning modes in spherical tokamaks: Multi-branch instabilities and effects beyond ideal MHD

Yueqiang Liu ; Chen Zhao ; Fatima Ebrahimi



*Phys. Plasmas* 32, 122507 (2025)
https://doi.org/10.1063/5.0305045
CHORUS

Physics of Plasmas ARTICLE pubs.aip.org/aip/pop

# Peeling-ballooning modes in spherical tokamaks: Multi-branch instabilities and effects beyond ideal MHD

Cite as: Phys. Plasmas **32**, 122507 (2025); doi: 10.1063/5.0305045
Submitted: 2 October 2025 · Accepted: 8 December 2025 ·
Published Online: 22 December 2025

View Online Export Citation CrossMark

Yueqiang Liu,[1,a)] Chen Zhao,[1] and Fatima Ebrahimi[2]

## AFFILIATIONS

[1]General Atomics, PO Box 85608, San Diego, California 92186-5608, USA
[2]Princeton Plasma Physics Laboratory, Princeton, New Jersey 08543, USA

[a)]Author to whom correspondence should be addressed: liuy@fusion.gat.com

## ABSTRACT

A number of important physics effects on the stability of relatively high-$n$ ($n$ is the toroidal mode number) peeling-ballooning modes (PBMs) are investigated based on an equilibrium reconstructed from a NSTX discharge, utilizing extended magnetohydrodynamic (MHD) eigenvalue solvers. For a given toroidal mode number $n$, multiple branches of instabilities are computed, with the total number of unstable branches roughly linearly scaling with $n$. Most of the unstable branches are located in the plasma core region, but edge-localized branches, i.e., PBMs, are also identified at higher $n$-numbers. For the single-fluid-wise most unstable PBM with $n = 19$, stabilizing/destabilizing effects due to various physics beyond ideal MHD are systematically investigated. Plasma toroidal flow is found to be weakly stabilizing. Local flow shear is generally stabilizing as well, with the degree of stabilization depending on the initial growth rate (without flow shear) of the mode. The plasma resistivity can strongly destabilize the PBM within the single-fluid framework. Anisotropic thermal transport, strong parallel sound wave damping, as well as two-fluid effects are all stabilizing to the mode. In particular, diamagnetic stabilization (within the two-fluid model) is found to be very strong for this mode.





## I. INTRODUCTION

Large bursts of edge-localized modes (ELMs) can induce severe material damage, in particular to the divertor surfaces, in future reactor-scale tokamak devices such as ITER.[1] Understanding ELM physics, as well as their control, is therefore of crucial importance. Significant progress has been made in both areas during recent years.[2] Overall, it is fair to state that (i) the onset physics of large, the so-called Type-I ELMs, is now well understood as associated with ideal peeling-ballooning modes (PBM).[3] Theoretical models, in particular the EPED model,[4] have been developed and well validated against experiments, especially for conventional tokamak devices.

On the other front, (ii) ELM control using the three-dimensional resonant magnetic perturbation (RMP) produced by external magnetic coils has reached a relatively mature level in both experiments[5] and with a reasonably good understanding of the associated edge-peeling plasma response physics.[6] This physics understanding has also recently been employed to systematically optimize the RMP spectrum for type-I ELM control in both conventional (ITER)[7] and low-aspect ratio (STEP)[8] reactor-scale devices.

Although linear ideal magnetohydrodynamic (MHD) theory, in combination with diamagnetic stabilization,[9] has been shown to be successful in predicting ELM onset in conventional aspect ratio tokamaks, effects of the plasma resistivity on the ballooning mode stability have been shown, both analytically[10–12] and numerically,[13–15] to play important roles as well. In particular, recent work appears to indicate that the plasma resistivity plays an important role in reconciling with the experimental observations in spherical tokamaks (STs), such as NSTX[16–18] and MAST-U.[19,20] Indeed, ideal MHD computations, including the diamagnetic effect, predicted stable PBMs in ELMy discharges in these devices. Resistive PBMs were thus identified as the instability responsible for type-I ELMs in these experiments, in conjunction with the diamagnetic effect. The latter was also shown to modify the stability of kink modes.[21,22]

This work aims to conduct a systematic investigation of the PBM stability in an ST device, focusing on physics effects beyond ideal MHD. We find that several interesting physics aspects can be clarified based on an equilibrium reconstructed from an ELMy H-mode experiment in NSTX. We emphasize that (i) physics understanding is our primary goal here, despite the fact that a realistic plasma equilibrium is

utilized. Hence, a direct comparison with experiments is of secondary importance in the present study. (ii) The present work only considers the linear stability of PBMs. Nonlinear modeling of (type-I) ELM dynamics in ST, such as that recently performed for MAST-U,[19] is beyond the scope of this study and is indeed beyond the code capability employed here.

The codes that we will use are the single-fluid, full MHD, linear eigenvalue solver MARS-F,[24] and its recent two-fluid extension MARS-2F.[25] The additional physics effects included in these codes are: (1) the plasma resistivity (the Spitzer model), (2) the plasma toroidal equilibrium flow and flow shear, (3) the plasma anisotropic thermal transport effect, (4) the parallel sound wave damping effect, and (5) the two-fluid effect.

The remainder of the work is organized as follows: Sec. II presents the NSTX equilibrium for the PBM stability analysis. Section III briefly introduces the modeling tools—the formulation behind the MARS-F and MARS-2F codes, as well as the aforementioned physics terms. Section IV reports multi-branch instabilities with or without plasma flow, followed by numerical convergence tests for the selected high-$n$ instability reported in Sec. V. Sensitivity studies, against individual variation of all the aforementioned plasma parameters (1)–(5), will be reported in Sec. VI. Section VII summarizes the work.

## II. EQUILIBRIUM

We consider an equilibrium reconstructed from the NSTX discharge 132543, with the magnetic geometry including the plasma boundary surface shown in Fig. 1(a). This is a type-I ELMy discharge, where it is believed that the ELM is peeling-limited. The wall shape is also shown here, where the ideal-wall boundary condition is applied in MARS-F computations reported later. Note that for PBMs of high mode frequency (due to fast plasma flow) studied here, the ideal-wall assumption should be a reasonable approximation. The safety factor profile has the on-axis value of about 0.95, and large edge values, as being typical for highly elongated spherical tokamak equilibria.

Figure 2 reports key equilibrium kinetic profiles, reconstructed over a small time-window during the inter-ELM period (covering the last 20% of the inter-ELM period at around 700 ms of the discharge).[17] The edge pedestal structures appear in all reconstructed kinetic profiles. In what follows, we will use the electron density profile [Fig. 2(b)]

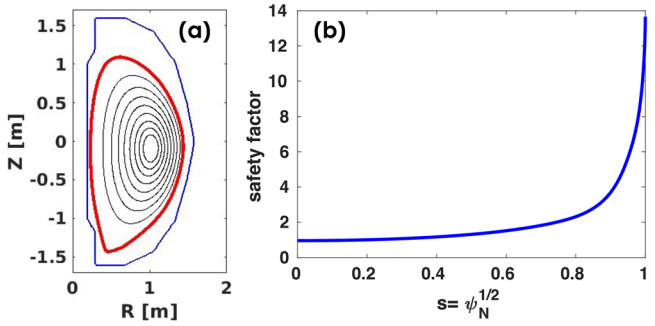


**FIG. 1.** Equilibrium reconstructed from the NSTX ELMy H-mode discharge 132543, showing (a) the plasma boundary shape (thick red line) together with representative flux surfaces (thin black lines) and the wall shape (blue), where the ideal-wall boundary condition is applied and (b) the safety factor profile. $\psi_N$ is the normalized equilibrium poloidal magnetic flux.

to calculate the plasma resistivity profile according to the Spitzer model.[23] We will also scan the on-axis value of the plasma toroidal rotation frequency [Fig. 2(d)] while keeping the overall shape of the radial profile fixed. We remark that the experimental flow is fast, in particular, in the plasma core. The flow correction to the plasma equilibrium, therefore, may not be negligible for the case considered. In the linear stability calculations reported in the present work, the flow correction to the plasma equilibrium is neglected.

## III. MODELING TOOLS

The modeling tools that we employ in the present work are the MARS-F[24] and MARS-2F[25] codes. In what follows, we present the model equations in a rather complete form, encompassing both the single- and two-fluid terms, as well as those key additional physics effects beyond ideal MHD, that we will individually consider in this study in the context of the PBM stability. The linear stability is formulated as an eigenvalue problem

$$p\tilde{\rho} + \nabla\cdot(\rho_0\tilde{\mathbf{v}}) + \nabla\cdot(\tilde{\rho}\mathbf{V}_0) = 0, \tag{1}$$

$$\rho_0\left[(p+in\bar{\Omega})\tilde{\mathbf{v}} + \underbrace{(\mathbf{V}_{*i},\nabla)\tilde{\mathbf{v}}_\perp}_{\text{FLR}}\right] = \tilde{\mathbf{j}}\times\mathbf{B}_0 + \mathbf{j}_0\times\tilde{\mathbf{B}} - \nabla\tilde{P} - \rho_0\left[2\bar{\Omega}\nabla Z\times\tilde{\mathbf{v}} + R^2(\tilde{\mathbf{v}}\cdot\nabla\bar{\Omega})\nabla\phi\right] - \tilde{\rho}R^2\bar{\Omega}^2\nabla Z\times\nabla\phi - \underbrace{\kappa_{||}|k_{||}|v_{th,i}\rho_0\tilde{\mathbf{v}}_{L||}}_{\text{PSWD}}, \tag{2}$$

$$(p+in\bar{\Omega})\tilde{\mathbf{B}} = \nabla\times(\tilde{\mathbf{v}}\times\mathbf{B}_0) + R^2(\tilde{\mathbf{B}}\cdot\nabla\bar{\Omega})\nabla\phi - \nabla\times(\eta\tilde{\mathbf{j}}) + \underbrace{\nabla\times\left[\frac{1}{en_0B_0^2}(\mathbf{B}_0\cdot\nabla\tilde{P}_e)\mathbf{B}_0\right] + \nabla\times\left[\frac{1}{en_0B_0^2}(\tilde{\mathbf{B}}\cdot\nabla P_{e0})\mathbf{B}_0\right]}_{\text{Hall}+\nabla p_e}, \tag{3}$$

$$(p+in\bar{\Omega})\tilde{P}_i + (\tilde{\mathbf{v}}\cdot\nabla P_{i0}) + \Gamma P_{i0}\nabla\cdot\tilde{\mathbf{v}} = \nabla_{||}\cdot(\chi_{||}\nabla_{||}\tilde{P}_i) + \nabla_\perp\cdot(\chi_\perp\nabla_\perp\tilde{P}_i) \underbrace{-2\Gamma\mathbf{V}_{Di}\cdot\nabla\tilde{P}_i}_{\text{reactive}-\text{closure}}, \tag{4}$$

$$(p+in\bar{\Omega})\tilde{P}_e + (\tilde{\mathbf{v}}\cdot\nabla P_{e0}) + \Gamma P_{e0}\nabla\cdot\tilde{\mathbf{v}} = \nabla_{||}\cdot(\chi_{||}\nabla_{||}\tilde{P}_e) + \nabla_\perp\cdot(\chi_\perp\nabla_\perp\tilde{P}_e), \tag{5}$$

$$\tilde{P} = \tilde{P}_i + \tilde{P}_e, \quad \tilde{\mathbf{j}} = \nabla\times\tilde{\mathbf{B}}, \tag{6}$$

where $p = \gamma + i\omega$ denotes the (complex) mode eigenvalue. $n$ is the toroidal mode number. Symbols with subscript "0" indicate the equilibrium quantities, and those with a tilde denote the corresponding perturbed quantities. Conventional notations are adopted for the plasma mass density ($\rho$), the fluid velocity ($\mathbf{v}$), the plasma current density ($\mathbf{j}$) and the magnetic field ($\mathbf{B}$), the thermal ion ($P_i$) and electron ($P_e$), as well as the total ($P$) pressure. $\mathbf{V}_0 = \mathbf{V}_{E\times B} + \mathbf{V}_{*i} = R^2\Omega\nabla\phi$ is the equilibrium toroidal fluid flow velocity, with $\mathbf{V}_{E\times B} = R^2\Omega_{E\times B}\nabla\phi$ being the equilibrium toroidal $E\times B$ flow velocity and $\mathbf{V}_{*i} \equiv \mathbf{B}_0\times\nabla P_{0i}/(Zen_0B_p^2)$ being the equilibrium diamagnetic flow velocity of thermal ions (the poloidal flow contribution is ignored). $\mathbf{V}_{Di} \equiv (T_{0i}/e)\nabla\times(\mathbf{B}_0/B_0^2)$ is the (averaged) equilibrium toroidal precession drift velocity of thermal ions. $\Gamma = 5/3$ is the ratio of specific heats. The equations are written here in cylindrical coordinates

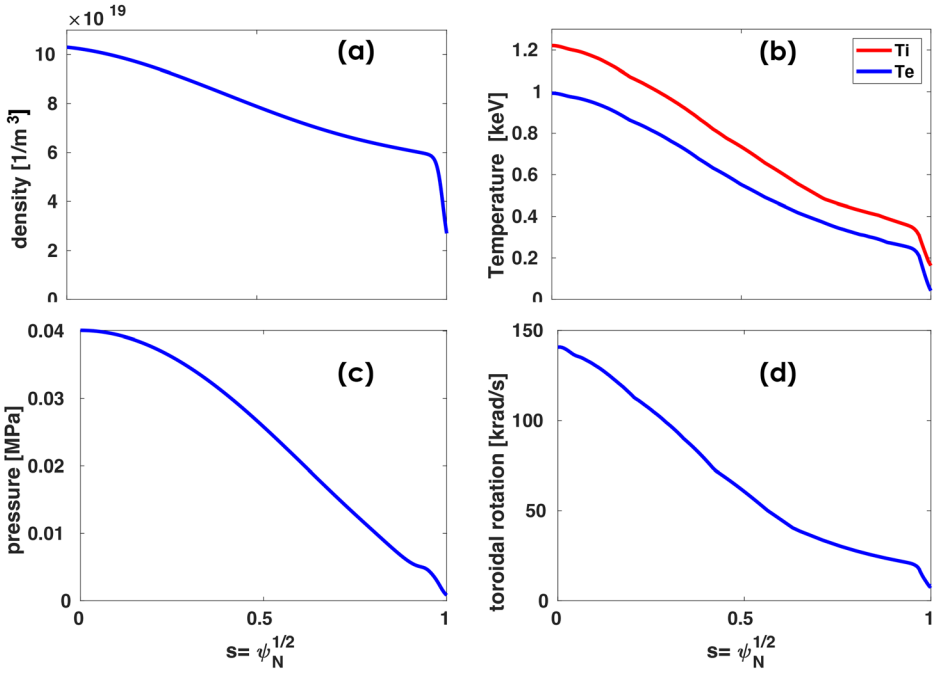


**FIG. 2.** Equilibrium kinetic profiles reconstructed for the NSTX discharge 132543, for (a) the plasma density, (b) the thermal ion ($T_i$) and electron ($T_e$) temperatures, (c) the plasma pressure, and (d) the fluid toroidal rotation frequency.

$(R, \phi, Z)$, although the MARS-F and MARS-2F implementations are eventually carried out in toroidal flux coordinates based on the equilibrium magnetic flux surfaces.

Detailed derivations of the above equations were reported in the Appendices of Ref. 26 (for inclusion of the toroidal fluid rotation with the MARS-F single-fluid formulation) and Ref. 25 (for the two-fluid formulation starting from the Braginskii model[27]). We start by discussing those underlined terms from the above equations. The last left-hand side (LHS) term from the momentum Eq. (2) is obtained after gyro-viscous cancelation and essentially represents the finite Larmor-radius (FLR) effect associated with the thermal ion diamagnetic flow. The last two terms from the right-hand side (RHS) of the induction Eq. (3) originate from the MHD Hall term combined (after certain partial cancelation) with the electron diamagnetic term due to $\nabla P_e$ in the extended Ohm's law. These two terms, together with the FLR term from Eq. (2), represent the key two-fluid physics.

Further extension is obtained by including the parallel sound wave damping (PSWD) model as the last RHS term in Eq. (2). This is a viscous force that damps the particle motion (i.e., the perturbed parallel velocity in the Lagrangian form $\tilde{\mathbf{v}}_L$) along the magnetic field line in a rotating plasma. The PSWD model mimics the thermal ion Landau damping physics as described by Hammett and Perkins.[28] Here, $v_{th,i}$ is the averaged thermal ion velocity (corresponding to the equilibrium thermal ion temperature $T_{i0}$), $k_{||}$ is the parallel wave number, and $\kappa_{||}$ a numerical coefficient specifying the damping strength. $\kappa_{||} \sim 1$ corresponds to strong PSWD.

The next unconventional term in the above model is the reactive closure term (the last RHS term) from the thermal ion energy Eq. (4). This closure term, which originated from the gyroviscous (or diamagnetic) heat flux to close the ion energy equation and is employed within the Weiland model,[29] is typically important for solving drift-wave problems. We include this closure here in order to examine its importance when applied to MHD problems.

The remaining terms from the above equations follow the conventional single-fluid formulation. The plasma resistivity ($\eta$) follows the Spitzer model. The anisotropic thermal transport is specified by the two diffusion coefficients $\chi_\perp$ and $\chi_{||}$ whose values vastly differ. Note that the parallel thermal conduction acts along the field lines in the presence of the perturbed magnetic field.[30]

In the MARS-2F code implementation, the terms associated with the FLR effect, the Hall and electron diamagnetic terms, as well as the reactive closure term, are all multiplied by a numerical coefficient $\alpha_{2F}$. The same parameter is also applied to define

$$\bar{\Omega} = \Omega - \alpha_{2F}\Omega_{*i}, \tag{7}$$

where $\Omega_{*i} = \mathbf{V}_{*i} \cdot \nabla\phi = -(dP_{0i}/d\psi_p)/(Zen_0)$ is for the toroidal component of the ion diamagnetic flow. At $\alpha_{2F} = 0$, we recover the single-fluid formulation from the above equations. The full two-fluid formulation is recovered in the limit of $\alpha_{2F} = 1$, where $\bar{\Omega} = \Omega_{E\times B}$. Equilibrium radial profiles for these various rotation frequencies are shown in Fig. 3, assuming the experimental toroidal fluid flow $\Omega = \Omega^{\text{expt.}}$. We remark that, unlike in other work,[9,17] we define $\Omega_{*i}$, in this study, without multiplication by the toroidal mode number $n$.

We also note that both the parallel and poloidal equilibrium flows are ignored in the above formulation. These flow options have also been implemented in MARS-F,[31,32] but are not activated in the present study. For the PBM stability analysis, we will consider the aforementioned physics effects individually, by scanning certain parameters (e.g., $\Omega, \eta, \kappa_{||}, \chi_\perp, \chi_{||}, \alpha_{2F}$) starting from a reference case.

## IV. MULTI-BRANCH INSTABILITIES

The eigenvalue solver allows identification of multiple unstable branches for the same toroidal mode number $n$. This is useful for

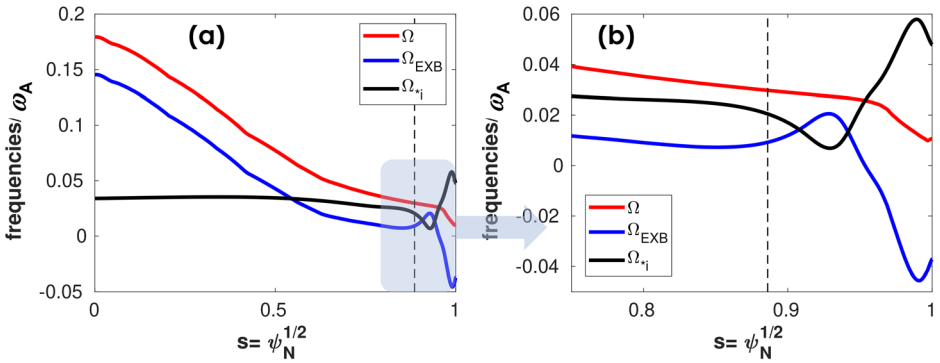


**FIG. 3.** Various toroidal rotation frequencies (the fluid rotation $\Omega$, $E \times B$ rotation $\Omega_{E\times B}$, and the thermal ion diamagnetic rotation $\Omega_{*i}$) for the NSTX discharge 132543, normalized by the toroidal Alfvén frequency $\omega_A$ and plotted in (a) the whole plasma region and (b) near the plasma edge. The vertical dashed line indicates the location of an $n = 19$ edge-localized instability.

(i) understanding the full (unstable) spectrum associated with an equilibrium, and perhaps more importantly (ii) finding out how various physics effects can lead to different dominant instability (one such example will be shown later). Figure 4(a) reports the MARS-F computed growth rates for different branches of unstable modes assuming vanishing equilibrium flow (thus vanishing mode frequency), while scanning the toroidal mode number $n$ from 1 to 20. As we will also show, these different branches have different radial locations inside the plasma.

It is interesting that the number of unstable roots, for a given mode number $n$, scales roughly linearly with $n$ [Fig. 4(b)]. This appears to indicate that the equilibrium safety factor plays an important role in dictating multiple unstable branches (the poloidal mode spectrum $m \sim nq$). We emphasize that not all branches are of the PBM nature. In fact, all 5 unstable branches with $n = 1$ are core-localized internal-kink-like modes (since $q_0 < 1$) satisfying the Sturmian property,[33] i.e., with subsequently increasing number of zero-crossings (the so-called node number) of the radial displacement as the mode growth rate decreases. Multiple branches at higher-$n$ can be located either in the plasma core or edge (examples to be shown later).

Note that we truncate the unstable spectrum at $\gamma/\omega_A < 10^{-3}$ here. There are typically several additional branches with very small growth rates, but we are generally not interested in these weakly unstable modes. This truncation is also the reason for the slightly non-monotonic behavior of the curve (at $n = 4$ and 19) shown in Fig. 4(b): the next unstable branch happens to have the growth rate just below the cutoff value of $\gamma/\omega_A = 10^{-3}$ for $n = 4$ and 19, in contrast to their neighboring harmonics.

The above unstable spectrum is computed assuming vanishing plasma flow. Next, we trace these multiple unstable branches for a given $n$-number while scanning the toroidal flow speed. Figure 5 shows one example for $n = 19$. Although all the initially unstable branches (at vanishing flow) have been traced, we show a few most unstable ones for clarity of the presentation here. It is evident that the flow stabilization/destabilization effect varies for different branches [Fig. 5(a)]. Complete stabilization, at the experimental rotation, is computed for several of the less-unstable branches.

The computed mode frequency generally increases in proportion to the assumed rotation frequency, due to the fact that the mode frequency is largely caused by the Doppler shift effect. The amount of the Doppler shift, however, depends on the mode location along the radial coordinate (and is obviously proportional to $n$). The core-localized branch experiences a larger Doppler shift since the flow is faster there [Fig. 2(d)]. Consequently, the computed mode frequency is larger for the core-localized branches as compared to the edge-localized counterpart. Therefore, examining the final mode frequency (at the experimental rotation) from Fig. 5(b) reveals the mode radial location. In particular, the branch indicated by arrows in the figure has the lowest mode frequency and is located near the plasma edge. This branch is thus most relevant to the ELMy behavior observed in the experiment. Later studies (Sec. VI) will therefore focus on this branch, while scanning various plasma/model parameters beyond ideal MHD.

We make two more comments before showing examples of the computed eigenmode structures for multiple branches. First, as evident from Fig. 5(a), the plasma flow changes the dominant unstable spectrum. At the experimental rotation, all the core-localized branches

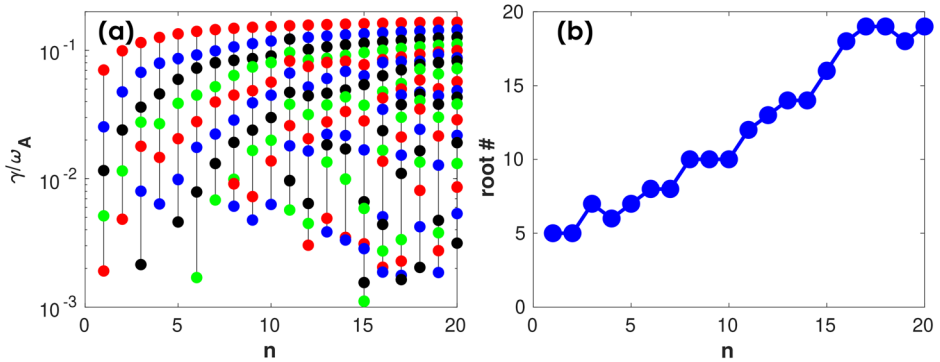


**FIG. 4.** The MARS-F computed (a) growth rates and (b) number of unstable roots, of multiple eigenmodes while scanning the toroidal mode number $n$. Assumed is the Spitzer model for the plasma resistivity and vanishing plasma equilibrium flow. Counted are only the unstable roots with the normalized growth rate $\gamma/\omega_A > 10^{-3}$.

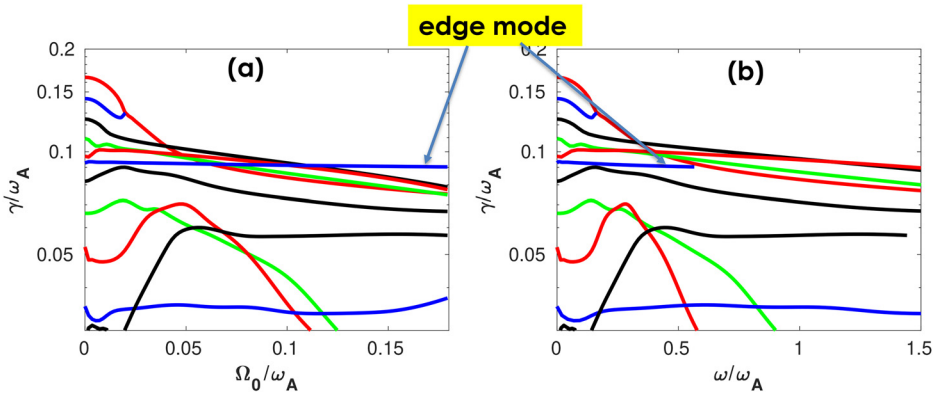


**FIG. 5.** The computed mode growth rate $\gamma$ vs (a) the on-axis value of the toroidal fluid rotation frequency $\Omega_0$ and (b) the computed mode frequency $\omega$, while scanning $\Omega_0$ from zero to the experimental value of $\Omega_0^{expt}/\omega_A = 0.179$. The radial profile shape of rotation is fixed, as shown in Fig. 2(d), while scanning the on-axis value. Shown is a portion of the unstable spectrum for the $n = 19$ modes with $\gamma/\omega_A > 0.03$ for better clarity of presentation. Similarly, the mode frequency is plotted up to $\omega/\omega_A = 1.5$ in (b). Indicated by arrows is also a branch localized near the plasma edge, with a relatively small mode frequency at the experimental rotation (the right-hand side end point of the curves).

are subject to stronger flow damping, leaving the edge-localized branch the most unstable. This branch is the *sixth* unstable one at vanishing flow. Second, mode conversion-merge occurs for certain branches while we increase the flow speed. This often happens in linear stability systems.[34] In the case shown here, the two most unstable branches (at vanishing flow) merge into one at a certain finite rotation frequency.

Figure 6 presents four examples of the computed $n = 19$ eigenmodes at the experimental rotation. It is evident that all branches are localized along the radial coordinate, but peak at different places. In particular, the edge-localized branch peaks at $s = \sqrt{\psi_N} = s_0 = 0.886$. Note that, as part of the eigenfunction, the overall amplitude of the pressure perturbation shown in the figure has no physics significance. The presence of a hole in the contour plots is due to the fact that the MARS-F computations were performed in an annular computational domain that excludes the plasma core region near the magnetic axis. This truncation is often helpful in reducing the computational challenge for high-$n$ modes located near the plasma edge. Numerical convergence with respect to the aforementioned truncation will be reported later on.

Figure 6(a) shows that the $n = 19$ edge instability, although being generally of a ballooning nature, still maintains certain peeling characteristics. Specifically, the perturbation is still significant near the top and bottom regions of the torus, and even extends toward the high-field side. Since this is the most unstable perturbation [cf. Fig. 5(a)], we may assume that this branch is responsible for the onset of the type-I ELMs observed in the NSTX experiment considered. Results reported later with the two-fluid model, however, show stability of the $n = 19$ edge branch. Nevertheless, a detailed investigation of this branch is carried out for physics understanding, to be reported in Secs. V and VI.

Figure 7 shows another example of the toroidal flow effect on the multi-branch instabilities, this time for a lower-$n$ ($n = 8$) spectrum. We again find both stabilizing and destabilizing effects of flow depending on the branch and the range of flow speed. As a consequence, flow changes the dominant unstable spectrum for the same toroidal mode

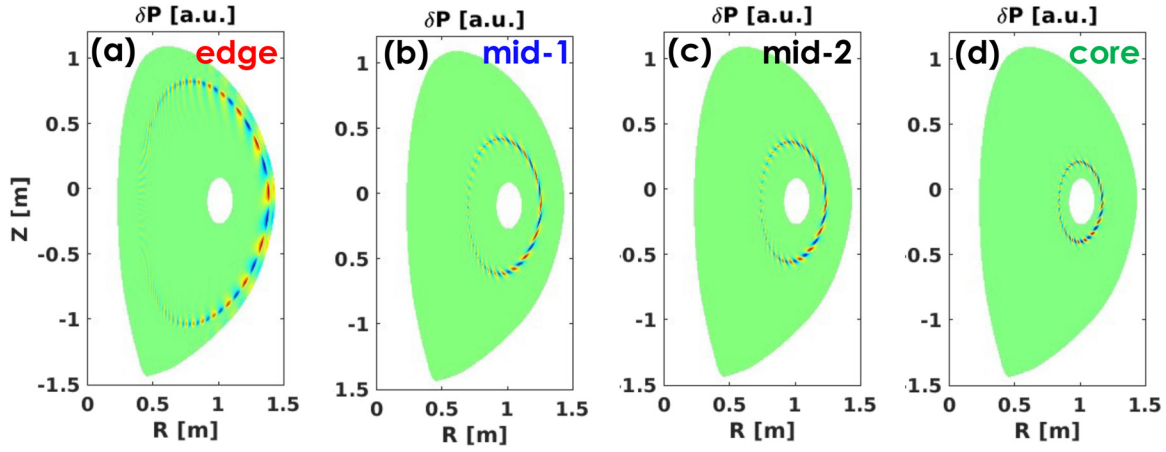


**FIG. 6.** The eigenmode structure in terms of the perturbed plasma pressure, plotted in the poloidal plane and compared among multiple unstable $n = 19$ modes located at (a) the plasma edge, (b) and (c) the middle of the plasma column, and (d) the plasma core region.

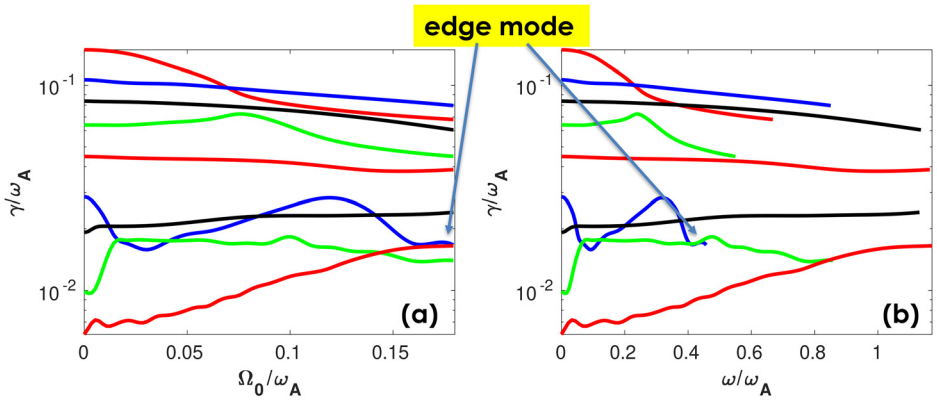


**FIG. 7.** The computed mode growth rate $\gamma$ vs (a) the on-axis value of the toroidal fluid rotation frequency $\Omega_0$ and (b) the computed mode frequency $\omega$, while scanning $\Omega_0$ from zero to the experimental value of $\Omega_0^{expt.}/\omega_A = 0.179$. The radial profile shape of rotation is fixed, as shown in Fig. 2(d), while scanning the on-axis value. Shown is the unstable spectrum for the $n = 8$ modes, with arrows indicating a branch with the smallest mode frequency (at the experimental rotation) and localized near the plasma edge.

number. For the case considered, most of the branches are core-localized. The one closest to the plasma edge, with the lowest mode frequency at the experimental flow, as indicated by arrows in the figure, peaks at $s_0 \simeq 0.6$, i.e., being less edge-localized than the $n = 19$ edge branch reported in Fig. 6(a). Given the additional fact that this branch is only moderately unstable, we will not perform a systematic calculation of various physics effects on the mode stability. Instead, we will focus more on the $n = 19$ edge-mode branch shown earlier, which is of the PBM nature and remains substantially unstable even at the experimental flow according to the single-fluid model.

In view of these flow-scan results, we again comment on the toroidal flow in NSTX. Although the toroidal flow is included in the perturbed MHD equations, the flow correction to the plasma equilibrium is ignored, as pointed out earlier. This is a significant approximation for the NSTX plasma considered, since the flow is fast. On the other hand, we are mostly interested in modes that are localized near the plasma edge, where the flow is relatively slow. At any rate, caution is needed when interpreting the experiment with the numerical results reported here.

## V. NUMERICAL CONVERGENCE

Before showing more physics results, we demonstrate numerical convergence of the results obtained. Since MARS-F utilizes spectral representation of the solution variables along the poloidal angle, a large number of poloidal Fourier harmonics is required for high-$n$ perturbations in order to achieve the converged eigenvalue (and eigenfunction). Figure 8 reports two examples ($n = 19$ and $n = 20$) where the eigenmodes peak near the plasma edge. The computed eigenvalues—both

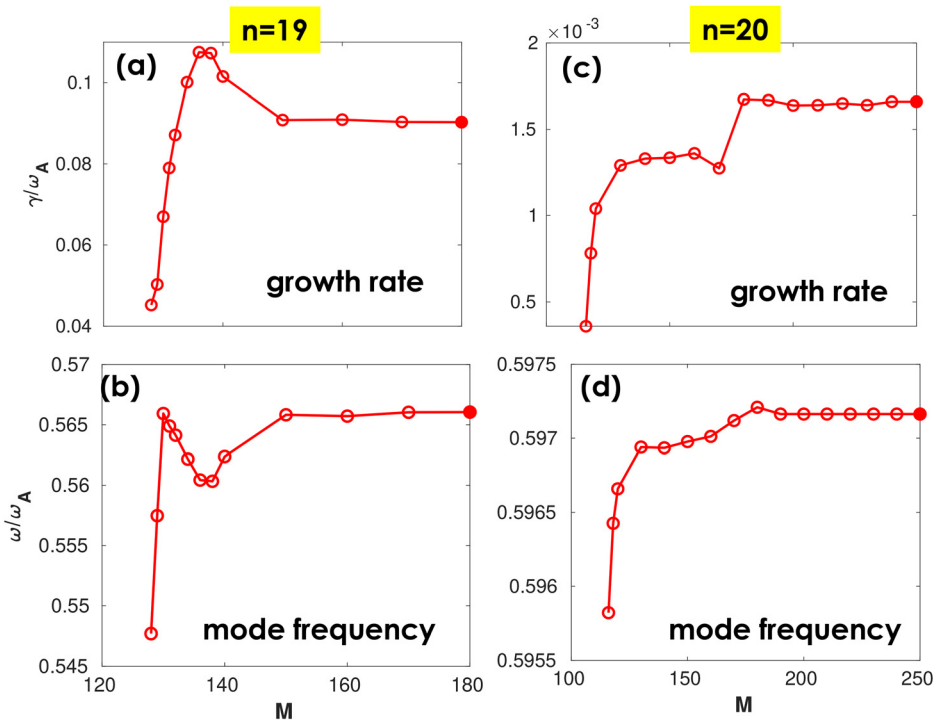


**FIG. 8.** Numerical convergence of the computed mode growth rate (top panels) and frequency (bottom panels) vs the total number ($M$) of poloidal Fourier harmonics included in MARS-F computations, for the (a) and (b) $n = 19$ and (c) and (d) $n = 20$ modes located near the plasma edge. The closed circle indicates the $M$-number adopted in default MARS-F runs.

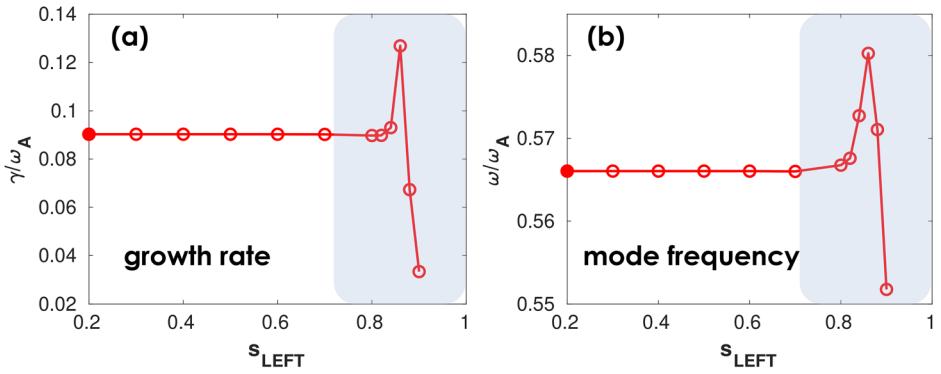


**FIG. 9.** Numerical convergence of the computed mode (a) growth rate and (b) frequency vs the truncation point of the computational domain from the left-hand side ($s_{LEFT}$) of the radial coordinate, for the $n = 19$ unstable branch located near the plasma edge. The shaded region indicates the region covered by the mode eigenfunction, as shown in Fig. 6(d). The closed circle indicates the $s_{LEFT}$-value adopted in default MARS-F runs.

growth rate and mode frequency—converge well with sufficiently large numbers ($M$) of the poloidal harmonics. The largest $M$-numbers here are used as the nominal values in further MARS-F computations.

On the poloidal convergence, we remark that a lower number of harmonics is needed for (i) lower-$n$ perturbations and (ii) modes localized in the plasma core region, where the safety factor $q$ is lower. This is because the required poloidal harmonics should roughly cover a range set by $m \sim nq$.

Figure 9 shows the numerical convergence of the MARS-F computed eigenvalue for the $n = 19$ edge branch, as we gradually increase the hole (indicated by the parameter $s_{LEFT}$) of the computational domain in the plasma core. The left-hand value here, $s_{LEFT} = 0.2$, corresponds to the nominal case shown in Fig. 6(a). It is evident that the numerical convergence is only lost when the computational domain inside the plasma no longer covers the region occupied by the mode eigenfunction. This region is shaded in Fig. 9. We should mention that while varying $s_{LEFT}$, the total number of radial mesh points inside the computational domain is kept the same. Figure 9, thus, to a certain degree, also illustrates the numerical convergence with respect to the radial resolution.

## VI. PHYSICS EFFECTS BEYOND IDEAL MHD

In what follows, we will scan various model parameters described in Sec. III, to understand physics effects beyond the ideal MHD assumption on the PBM instability. For the purpose of systematic investigations, we define a reference case as the MARS-F single-fluid model, the Spitzer resistivity, the experimental toroidal fluid rotation profile, vanishing parallel sound wave damping in the perturbed momentum equation, and vanishing thermal transport in the perturbed pressure equations. Sensitivity study against variation of each of

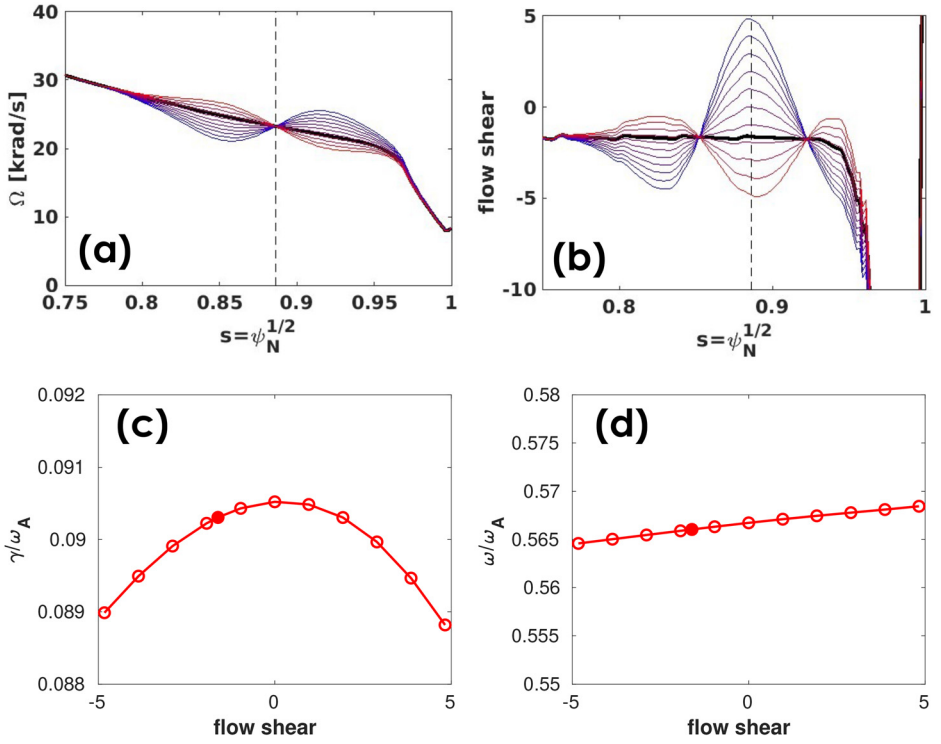


**FIG. 10.** Local variation of the (a) toroidal fluid flow profile and (b) the corresponding flow shear near the plasma edge, resulting in the change of the computed mode (c) growth rate, and (d) frequency for the $n = 19$ edge-localized unstable branch. The vertical dashed lines in (a) and (b) indicate the radial location where the mode eigenfunction peaks [cf. Fig. 6(a)]. The thick black lines in (a) and (b) and the closed circles in (c) and (d) indicate the experimental rotation profile.

the aforementioned physics will then be performed (mainly) for the $n = 19$ PBM branch, starting from the reference case. The $n = 19$ PBM branch is also found to be the most unstable among other $n$'s when the experimental flow is included in the MARS-F computation.

The effect of the toroidal flow was already reported in Sec. IV, which is stabilizing for the $n = 19$ PBM, albeit at a moderate level. Next, we consider the effect of flow shear on the computed mode stability (Fig. 10). We locally vary the flow shear at the radial location of the $n = 19$ eigenmode, without modifying the flow amplitude at the mode peak location $s_0 = 0.886$ [Fig. 10(a)], by introducing the following analytic function:

$$\Omega_{\text{new}}(s) = \Omega_{\text{expt}}(s) + \delta_S(s - s_0)\exp\left[-\frac{(s - s_0)^2}{\delta_0^2}\right], \qquad (8)$$

where $\Omega_{\text{expt}}$ is the experimental rotation profile as reported in Fig. 2(d). $\Omega_{\text{new}}$ is the modified profile. The Gaussian width $\delta_0 = 0.05$ is chosen to approximately cover the radial extension of the $n = 19$ PBM eigenfunction. The parameter $\delta_S$ is then scanned to modify the local flow shear, defined as $s(d\Omega/ds)/\Omega$.

MARS-F finds that, for the case considered, local flow shear [Fig. 10(b)] stabilizes the mode [Fig. 10(c)] with minor influence on the mode frequency [Fig. 10(d)]. Note that (i) the flow shear stabilization effect is generally weak here, and (ii) the sign of the flow shear does not matter. An early analytic calculation[35] showed that the pressure associated with the toroidal flow—essentially due to the centrifugal force—effectively enhances the plasma pressure toward the low-field side of the torus. The resulting flow shear, together with the equilibrium pressure gradient, acts against magnetic curvature for the ballooning drive. Consequently, a positive flow shear would compensate for the (generally negative) pressure gradient, resulting in a reduced interchange/ballooning drive in the bad curvature region. This leads to the (positive) flow shear stabilization of the ballooning mode. In our case, surprisingly, we also find flow shear stabilization, albeit weak, with negative shear. This may be due to the fact that the $n = 19$ perturbation computed here is not of a true ballooning nature. The eigenmode indeed extends out to the good-curvature region, as shown in Fig. 6(a).

The stabilizing effect of flow shear on the n = 19 PBM appears weak because the mode is already highly unstable. The effect becomes stronger for less unstable modes. One example is reported by Fig. 11 for the $n = 18$ PBM branch. In this case, a local negative flow shear of $-5$ (at the mode-peak location) reduces the mode growth rate by a factor of 3, compared to the vanishing flow shear case. The flow shear stabilization is, however, less symmetric with respect to the vanishing shear case between the positive and negative values.

Next, we consider the role of the plasma resistivity, which has been shown to be a critical factor in interpreting the ELMy H-mode experiments for NSTX.[17] Similar to the finding reported in the quoted work here, MARS-F single-fluid computations find that the plasma resistivity can strongly destabilize PBMs by assuming large plasma resistivity values (Fig. 12). Assuming the Spitzer value (indicated by the closed circle in Fig. 12), the enhancement of the mode growth rate is, however, moderate for the $n = 19$ edge branch. This is largely due to the fact that the mode considered here is unstable, even assuming an ideal plasma. This is different from a situation where the mode is

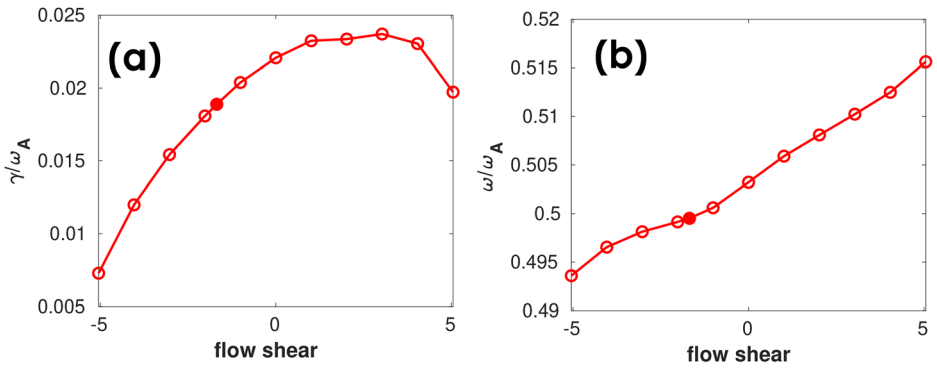


**FIG. 11.** The computed (a) growth rate and (b) mode frequency for the $n = 18$ edge-localized unstable branch, while scanning the local flow shear around the experimental value indicated by the closed circle.

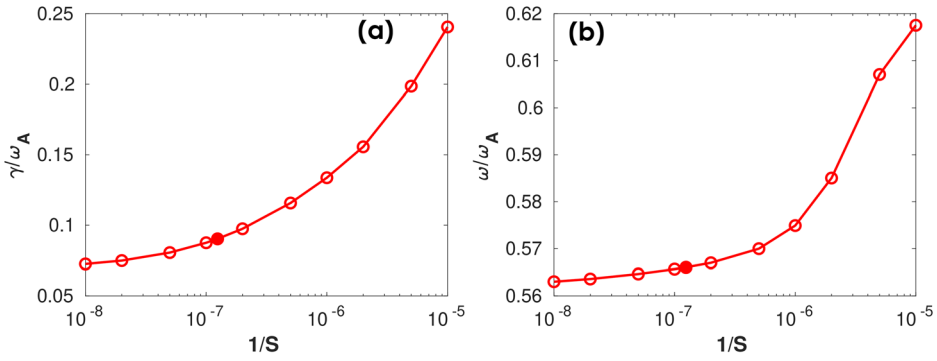


**FIG. 12.** The computed (a) growth rate and (b) mode frequency of the $n = 19$ edge-localized branch while varying the plasma resistivity (measured by the on-axis inverse Lundquist number $1/S$). The closed circle indicates the Spitzer value for the NSTX plasma considered. The shape of the radial profile of the plasma resistivity is fixed, following the $T_e^{-3/2}$-dependence while varying the on-axis value. Assumed is the experimental toroidal rotation.

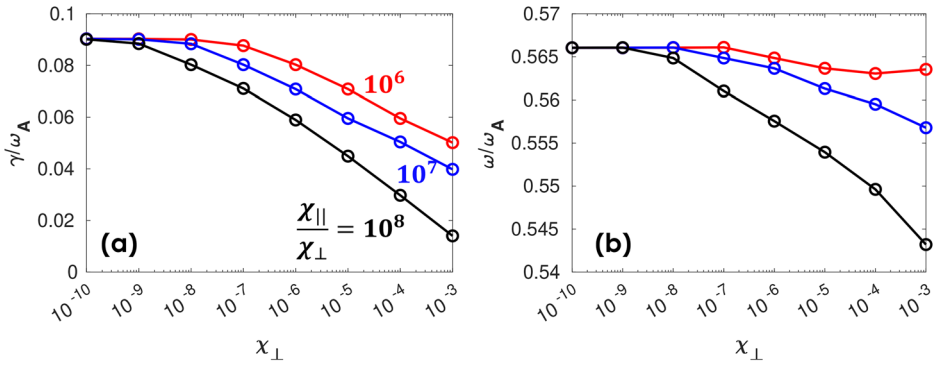


**FIG. 13.** The computed (a) growth rate and (b) mode frequency of the $n = 19$ edge-localized branch while varying the anisotropic thermal transport coefficients. The ratio of the parallel ($\chi_{||}$) to perpendicular ($\chi_\perp$) thermal diffusion coefficients are fixed (at three different values $10^6, 10^7, 10^8$) while scanning $\chi_\perp$. Both $\chi_{||}$ and $\chi_\perp$ are assumed to be constants along the radial coordinate and normalized by $\chi_0 = R_0^2/\tau_A$. The reference case corresponds to $\chi_\perp = 0$.

ideally stable but driven unstable by the plasma resistivity. On the other hand, we note that diamagnetic stabilization is not taken into account here (within the single fluid model). As a consequence of the resistive instability, magnetic islands are present near mode rational surfaces. However, the eigenvalue solution does not determine the island size (which is proportional to the square root of the resonant radial magnetic field) since the overall amplitude of the eigenfunction is arbitrary.

We now investigate the role of the plasma thermal transport in the mode stability. Figure 13 reports the computed mode eigenvalues while scanning both the (normalized) perpendicular ($\chi_\perp$) and parallel ($\chi_{||}$) thermal diffusion coefficients, while keeping the ratio $\chi_{||}/\chi_\perp$ fixed at three different values ($\chi_{||}/\chi_\perp = 10^6, 10^7, 10^8$). This range of scans covers the thermal transport regimes in typical tokamak plasmas. Note again that the reference case corresponds to vanishing thermal transport. It is evident from Fig. 13(a) that (i) enhancing thermal transport in general strongly stabilizes the mode considered and (ii) larger anisotropies of the thermal diffusion also yield stronger stabilization. The effect of the anisotropic thermal transport on the mode frequency is found to be limited [Fig. 13(b)].

It appears that the effect of the anisotropic thermal transport, though ultimately modifying the sound wave propagation, can be either stabilizing, e.g., for the high-$n$ resistive PBM as shown here, or destabilizing, e.g., for the (resistive) tearing mode.[36,37] The latter is largely due to the fact that thermal transport is effective in compensating the average favorable curvature stabilization in a toroidal plasma.[38]

Figure 14 reports the effect of the PSWD on the PBM, where we scan the damping strength coefficient $\kappa_{||}$. This effect has been shown to be generally stabilizing for low-frequency MHD modes such as the resistive wall mode.[39] For the plasma response to the RMP, the strong PSWD model (with $\kappa_{||} \sim 1$) yields a better agreement with the internal plasma perturbation measurement in the experiment.[40] Here, we also find the stabilizing, albeit weak, role of the strong PSWD in the $n = 19$ PBM. A peculiar feature, however, is the destabilizing effect near $\kappa_{||} = 0$ (i.e., the reference case). We interpret this as a consequence of the PSWD, while interacting with sound waves, effectively reducing the plasma inertial enhancement (the Pfirsch–Schlüter factor[41]). The latter is known to reduce the MHD mode growth rate. More precisely, this inertial enhancement factor introduces a jump in the mode growth rate when the plasma equilibrium pressure changes from zero to a small finite value.[42] This reduction of the inertia enhancement likely becomes prominent only for high-$n$ perturbations. We emphasize that, for our case, the PSWD effect is weak on both the mode growth rate and frequency.

We emphasize also that the ultimate physics of both the PSWD effect discussed above and the anisotropic thermal transport effect reported in Fig. 13 relies on the change of the parallel sound wave propagation inside the plasma.[43] The change thus can only occur at a finite equilibrium pressure, which allows sound wave propagation.

Finally, we consider the two-fluid effects on the $n = 19$ PBM. Figure 15 shows the MARS-2F computed mode eigenvalue, where we scan the numerical parameter $\alpha_{2F}$ introduced in Sec. III. Note that the limit of $\alpha_{2F} = 0$ corresponds to the single-fluid model (the reference case). The mode becomes stable before reaching the two-fluid limit of $\alpha_{2F} = 1$. In other words, the $n = 19$ PBM is found to be stable with our two-fluid model. The computed mode frequency decreases with

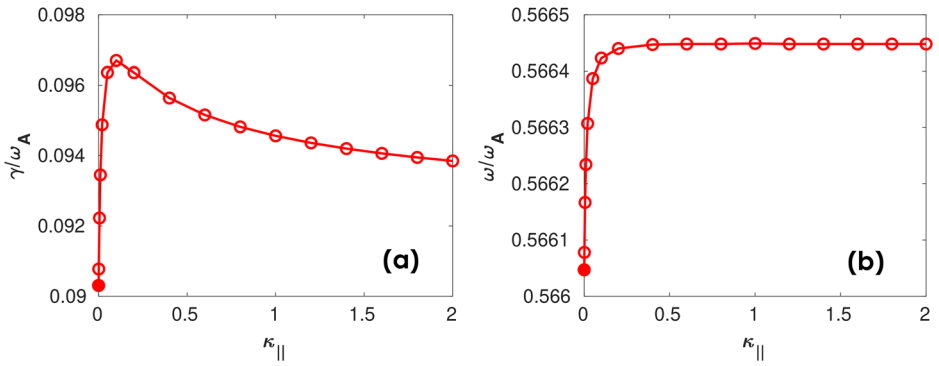


**FIG. 14.** The computed (a) growth rate and (b) mode frequency of the $n = 19$ edge-localized branch while scanning the numerical coefficient $\kappa_{||}$ for the parallel sound wave damping (PSWD) model. The closed circle (i.e., with vanishing PSWD) corresponds to the reference case.

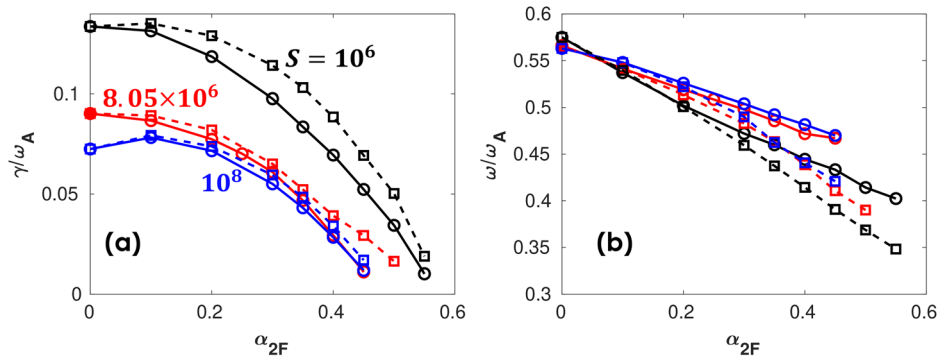


**FIG. 15.** The MARS-2F computed (a) growth rate and (b) mode frequency of the $n = 19$ edge-localized branch while scanning the numerical parameter $\alpha_{2F}$. $\alpha_{2F} = 0$ corresponds to the single-fluid limit while $\alpha_{2F} = 1$ being the two-fluid limit. Varied here is also the plasma resistivity, with the corresponding on-axis Lundquist number $S = 10^6$ (black), $8.05 \times 10^6$ (red, the Spitzer value), and $10^8$ (blue), respectively. Compared are also the two-fluid models with (solid lines) and without (dashed lines) the reactive closure term in the thermal ion energy equation. The closed circle indicates the reference case with the single-fluid model.

$\alpha_{2F}$, but remains positive (i.e., following the ion diamagnetic direction) as long as the mode is unstable [Fig. 15(b)].

This two-fluid stabilization, essentially due to the diamagnetic effect (often referred to as the FLR effect), appears to be robust against the variation of the plasma resistivity. Considered here are three different (on-axis) Lundquist numbers $S = 10^6, 10^8$, and $8.05 \times 10^6$, with the latter corresponding to the Spitzer resistivity evaluated for the NSTX plasma considered. A variant of the two-fluid model, where we remove the reactor closure term from Eq. (4), produces similar results as indicated by dashed-line curves in the figure. We emphasize that the ion gyroviscous term, which was found to be destabilizing to the interchange mode for a certain class of plasma equilibria,[44,45] is effectively included in the MARS-2F formulation (but partially canceled by the parallel component of the Reynolds stress tensor terms associated with the ion diamagnetic flow).[25]

It is interesting to compare with the approximate rule for diamagnetic stabilization of the ballooning mode: $n\omega_{*i}/2 > \gamma_0$,[9] where $\gamma_0$ is the ballooning mode growth rate according to the single-fluid (ideal MHD) calculation. In our case, $\gamma_0 = 0.093\omega_A$ (at vanishing flow and assuming Spitzer resistivity), $\omega_{*i} = 0.021\omega_A$ at the mode location ($s = 0.886$, indicated by the vertical dashed line in Fig. 3). This leads to $n\omega_{*i}/2 \sim 0.2\omega_A > \gamma_0$. The numerical result here is thus consistent with the analytic rule for the diamagnetic stabilization.

Two-fluid stabilization of the (relatively) high-$n$ modes begs the question of interpreting the experimental data, where the discharge was observed in the ELMy H-mode regime. It turns out that the lower-$n$ modes can remain unstable even with the two-fluid model. We show this again for the $n = 8$ instability (cf. Fig. 7), but this time, only considering the branch that is located nearest to the plasma edge. The corresponding mode eigenvalues and (examples of) eigenfunctions are reported in Fig. 16. For the branch that is unstable at the single-fluid limit ($\alpha_{2F} = 0$), the two-fluid effect is initially stabilizing at a certain range of $\alpha_{2F}$ (=0.12–0.36), as shown by the red curve (Root-1) in Fig. 16(a). This trend is, however, terminated by the appearance of another unstable root (Root-2), which is stable in the single-fluid limit ($\alpha_{2F} = 0$) but unstable in the two-fluid limit ($\alpha_{2F} = 1$). Interestingly, the eigenvalues of both roots merge at $\alpha_{2F} = 0.36$. We, thus, postulate that the second unstable root here (in the physical limit of $\alpha_{2F} = 1$),

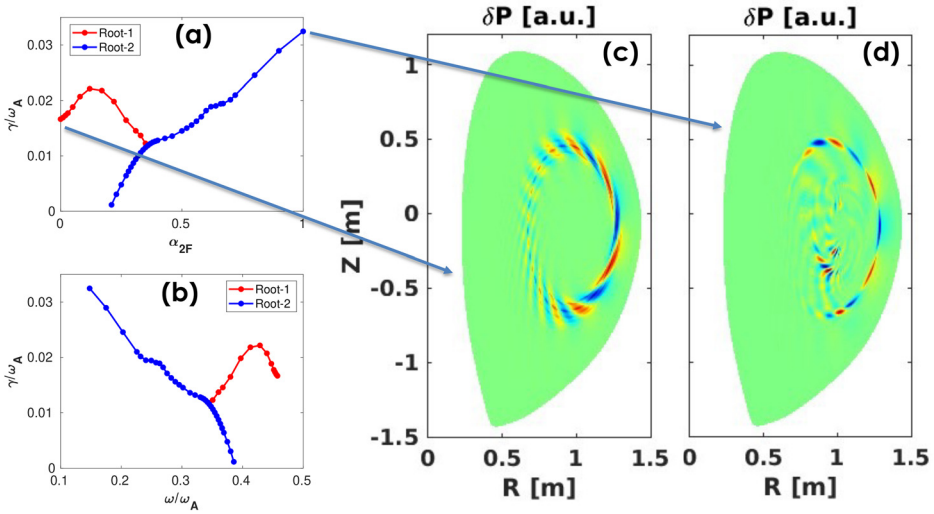


**FIG. 16.** The MARS-2F computed $n = 8$ mode (a) growth rate, (b) frequency, and (c) and (d) eigenfunctions (in terms of the perturbed pressure) for the branch located nearest to the plasma edge, while scanning the numerical parameter $\alpha_{2F}$. Shown in (c) is the eigenmode corresponding to the single-fluid limit ($\alpha_{2F} = 0$) while in (d), the two-fluid limit with reactive closure is also included ($\alpha_{2F} = 1$). Assumed are the Spitzer resistivity model and the experimental plasma rotation.

"triggered" by the two-fluid effect, can be responsible for the experimentally observed ELMs in the NSTX discharge considered. The MHD Hall term is likely the driver for the instability, although this is not easy to verify within our formulation, since the former is not separated from the diamagnetic term in Eq. (3) due to the partial cancelation effect mentioned earlier. We also remark that the second unstable branch (in blue) is triggered at vanishing frequency [Fig. 16(b)]. In other words, the mode would rotate in the electron diamagnetic direction were it stable.

The mode is not located right at the plasma edge, though [Fig. 16(d)]. Compared to the single-fluid counterpart [Fig. 16(c)], some perturbations also occur in the plasma core for the two-fluid triggered instability. A detailed examination of the evolution of the eigenmode structure, while scanning $\alpha_{2F}$, reveals that the mode is largely core-localized (near the radial coordinate of $s = 0.3$) when triggered, i.e., at $\alpha_{2F} \sim 0.2$. This core mode then gradually shifts outwards with increasing $\alpha_{2F}$. The physically relevant eigenmode shown in Fig. 16(d) still partly couples to certain core activity. Such a "mixed" mode structure is, however, robust—a very similar result is obtained, e.g., also at $\alpha_{2F} = 0.8$. Experimentally, such a core activity may be observable by measuring the plasma core flow damping.

The above "triggering" nature is further confirmed by considering the analytic diamagnetic stabilization rule mentioned earlier. The diamagnetic frequency at the peak location of the $n = 8$ instability is $\omega_{*,i}/\omega_A = 3.26 \times 10^{-2}$, leading to a much larger value of $n\omega_{*i}/2$ ($n = 8$ here), as compared to the single-fluid growth rate of $\gamma/\omega_A = 1.67 \times 10^{-2}$ with experimental flow or $\gamma/\omega_A = 2.86 \times 10^{-2}$ without flow. In other words, the analytic rule would predict full two-fluid stabilization of the $n = 8$ mode here, thus cannot explain the experimental observation. We nevertheless remark again that direct comparison/interpretation of experiment is not the focus of the present investigation, which aims to understand physics effects beyond ideal MHD on relatively high-$n$ PBMs.

## VII. CONCLUSION AND DISCUSSION

Based on an equilibrium reconstructed from the NSTX ELMy H-mode discharge, we investigate a number of important physics effects on the stability of relatively high-$n$ PBMs, utilizing the MARS-F and MARS-2F eigenvalue codes. For a given toroidal mode number $n$, multiple branches of instabilities are computed for this NSTX plasma. The total number of unstable branches (at vanishing plasma flow) is found to scale roughly linearly with $n$. Most of the unstable branches are located in the plasma core region, but edge-localized branches, i.e., PBMs, are also identified at higher $n$-numbers.

For the purpose of physics understanding, we focus on a representative PBM mode with $n = 19$, which is also the most unstable mode, among different $n$'s according to the single-fluid model, that is localized in the plasma edge region. Stabilizing/destabilizing effects on this branch, due to various physics beyond ideal MHD, are systematically investigated with results summarized in Table I. Plasma toroidal flow is found to be stabilizing for this PBM branch, although it can also be destabilizing for other branches. As a consequence, we find that the plasma flow modifies the dominant unstable spectrum of the equilibrium considered. Local flow shear is found to be generally stabilizing for the PBM, with the degree of stabilization depending on the initial growth rate (without flow shear) of the mode. The plasma resistivity can strongly destabilize the PBM within the single-fluid framework. Anisotropic thermal transport, strong parallel sound wave damping, as well as two-fluid effects are all stabilizing to the mode. In particular, diamagnetic stabilization (within the two-fluid model) is found to be very strong for the plasma considered—the $n = 19$ PBM is predicted to be fully stable by MARS-2F.

**TABLE I.** Summary of various physics effects on high-$n$ PBM stability in NSTX, as computed by the MARS-F and MARS-2F models.

| Physics terms | Effect | Degree of effect |
|---|---|---|
| Toroidal flow | Stabilizing | Weak |
| Toroidal flow shear | Stabilizing | Moderate |
| Plasma resistivity | Destabilizing | Strong |
| Thermal transport | Stabilizing | Strong |
| Weak PSWD | Destabilizing | Weak |
| Strong PSWD | Stabilizing | Weak |
| Two-fluid | Stabilizing | Strong |
| Reactive closure | Destabilizing | Weak |

Although direct comparison with experiment is of secondary consideration in the present work, we nevertheless discuss this aspect here. As mentioned earlier, the two-fluid model predicts complete stability of the higher-$n$ PBMs for this ELMy H-mode plasma. On the other hand, two-fluid effects can destabilize/trigger lower-$n$ modes, which may explain the ELMy behvaior in the discharge studied. It is, however, important to bear in mind that the flow correction to the plasma equilibrium is neglected in the present study. Despite being a less severe issue for modes localized near the plasma edge (where the flow is much slower), this is still a significant approximation for the NSTX plasma. The effect of the exact X-point geometry is not studied here due to limitations of the numerical implementation. The X-point geometry has been shown to be stabilizing on the kink-peeling mode.[46] Furthermore, other physics effects beyond two-fluid, e.g., nonlinear MHD, or perhaps two-fluid but combined with a flowing equilibrium, are needed to more consistently describe the ELMy H-mode experiment in NSTX. Kinetic effects may offer another possibility, which will be studied in the future, utilizing the MARS-K code.[47]

## ACKNOWLEDGMENTS

This material is based upon work supported by the U.S. Department of Energy, Office of Science, Office of Fusion Energy Sciences, under Award Nos. DE-AC02-09CH11466 and DE-FG02-95ER54309. This research used resources of the OLCF, which is an Office of Science User Facility supported under Contract No. DE-AC05-00OR22725.

This report was prepared as an account of work sponsored by an agency of the United States Government. Neither the United States Government nor any agency thereof, nor any of their employees, makes any warranty, express or implied, or assumes any legal liability or responsibility for the accuracy, completeness, or usefulness of any information, apparatus, product, or process disclosed, or represents that its use would not infringe privately owned rights. Reference herein to any specific commercial product, process, or service by trade name, trademark, manufacturer, or otherwise, does not necessarily constitute or imply its endorsement, recommendation, or favoring by the United States Government or

any agency thereof. The views and opinions of authors expressed herein do not necessarily state or reflect those of the United States Government or any agency thereof.

## AUTHOR DECLARATIONS

### Conflict of Interest

The authors have no conflicts to disclose.

### Author Contributions

**Yueqiang Liu:** Conceptualization (lead); Data curation (lead); Formal analysis (lead); Funding acquisition (lead); Investigation (lead); Methodology (lead); Project administration (lead); Resources (lead); Software (lead); Supervision (lead); Validation (lead); Visualization (lead); Writing – original draft (lead); Writing – review & editing (equal). **Chen Zhao:** Formal analysis (equal); Investigation (equal); Writing – review & editing (equal). **Fatima Ebrahimi:** Conceptualization (equal); Funding acquisition (equal); Project administration (equal); Resources (equal); Writing – review & editing (equal).

## DATA AVAILABILITY

The data that support the findings of this study are available from the corresponding author upon reasonable request.

## REFERENCES


[1]A. Loarte, G. Huijsmans, S. Futatani, L. R. Baylor, T. E. Evans, D. M. Orlov, O. Schmitz, M. Becoulet, P. Cahyna, Y. Gribov *et al.*, Nucl. Fusion **54**, 033007 (2014).
[2]M. E. Fenstermacher, L. R. Baylor, E. de la Luna, M. G. Dunne, G. T. A. Huijsmans, A. Kirk, F. M. Laggner, T. H. Osborne, C. Paz-Soldan, S. Saarelma *et al.*, Nucl. Fusion **65**, 053001 (2025).
[3]P. B. Snyder, H. R. Wilson, J. R. Ferron, L. L. Lao, A. W. Leonard, T. H. Osborne, A. D. Turnbull, D. Mossessian, M. Murakami, and X. Q. Xu, Phys. Plasmas **9**, 2037 (2002).
[4]P. B. Snyder, R. J. Groebner, A. W. Leonard, T. H. Osborne, and H. R. Wilson, Phys. Plasmas **16**, 056118 (2009).
[5]T. E. Evans, Plasma Phys. Controlled Fusion **57**, 123001 (2015).
[6]Y. Q. Liu, A. Kirk, Y. Gribov, M. P. Gryaznevich, T. C. Hender, and E. Nardon, Nucl. Fusion **51**, 083002 (2011).
[7]L. Li, Y. Q. Liu, A. Loarte, S. D. Pinches, A. Polevoi, Y. Liang, and F. C. Zhong, Nucl. Fusion **59**, 096038 (2019).
[8]Y. Q. Liu, X. Chen, Z. Y. Li, S. Saarelma, T. F. Tang, and G. L. Xia, Plasma Phys. Controlled Fusion **67**, 085010 (2025).
[9]P. B. Snyder, R. J. Groebner, J. W. Hughes, T. H. Osborne, M. Beurskens, A. W. Leonard, H. R. Wilson, and X. Q. Xu, Nucl. Fusion **51**, 103016 (2011).
[10]H. R. Strauss, Phys. Fluids **24**, 2004 (1981).
[11]J. W. Conner, R. J. Hastie, and T. J. Martin, Plasma Phys. Controlled Fusion **27**, 1509 (1985).
[12]A. Sykes, C. M. Bishop, and R. J. Hastie, Plasma Phys. Controlled Fusion **29**, 719 (1987).
[13]B. J. Burke, S. E. Kruger, C. C. Hegna, P. Zhu, P. B. Snyder, C. R. Sovinec, and E. C. Howell, Phys. Plasmas **17**, 032103 (2010).
[14]T. Y. Xia, X. Q. Xu, and P. W. Xi, Nucl. Fusion **53**, 073009 (2013).
[15]S. J. P. Pamela, G. T. A. Huijsmans, T. Eich, S. Saarelma, I. Lupelli, C. F. Maggi, C. Giroud, I. T. Chapman, S. Smith, L. Frassinetti *et al.*, Nucl. Fusion **57**, 076006 (2017).
[16]A. Kleiner, N. M. Ferraro, A. Diallo, and G. Canal, Nucl. Fusion **61**, 064002 (2021).
[17]A. Kleiner, N. M. Ferraro, G. Canal, A. Diallo, and R. Maingi, Nucl. Fusion **62**, 076018 (2022).
[18]A. Pankin, F. Ebrahimi, J. King, A. Kleiner, and J. Dominguez-Palacios, Plasma Phys. Controlled Fusion **67**, 095023 (2025).
[19]T. F. Tang, Y. Q. Liu, J. Stobbs, and J. R. Harrison, Plasma Phys. Controlled Fusion **67**, 085015 (2025).
[20]A. Kleiner, K. Imada, F. Ebrahimi, N. M. Ferraro, S. R. Haskey, L. Kogan, and A. Pankin, Plasma Phys. Controlled Fusion **67**, 085026 (2025).
[21]F. D. Halpern, D. Leblond, H. Lutjens, and J.-F. Luciani, Plasma Phys. Controlled Fusion **53**, 015011 (2011).
[22]Y. Zhang, W. Zhang, L. Q. Xu, X. D. Meng, and Z. W. Ma, Nucl. Fusion **65**, 076030 (2025).
[23]R. S. Cohen, L. Spitzer, and P. M. Routly, Phys. Rev. **80**, 230 (1950).
[24]Y. Q. Liu, A. Bondeson, C. M. Fransson, B. Lennartson, and C. Breitholtz, Phys. Plasmas **7**, 3681 (2000).
[25]X. Yang, Y. Q. Liu, L. Li, J. Yuan, X. He, Y. L. He, G. L. Xia, and G. Q. Dong, Nucl. Fusion **65**, 076019 (2025).
[26]X. Sun, Y. Q. Liu, L. L. Lao, C. Paz-Soldan, and J. Milliano, Phys. Plasmas **31**, 013902 (2024).
[27]S. I. Braginskii, Rev. Plasma Phys. **1**, 205 (1965).
[28]G. W. Hammett and F. W. Perkins, Phys. Rev. Lett. **64**, 3019 (1990).
[29]J. Weiland, A. B. Jarmen, and H. Nordman, Nucl. Fusion **29**, 1810 (1989).
[30]X. Bai, Y. Q. Liu, and Z. Gao, Phys. Plasmas **24**, 102505 (2017).
[31]G. L. Xia, Y. Q. Liu, L. Li, C. J. Ham, Z. R. Wang, and S. Wang, Nucl. Fusion **59**, 126035 (2019).
[32]L. Li, Y. Q. Liu, A. Loarte, O. Schmitz, Y. F. Liang, and F. C. Zhong, Phys. Plasmas **25**, 082512 (2018).
[33]J. P. Goedbloed and P. H. Sakanaka, Phys. Fluids **17**, 908 (1974).
[34]S. X. Yang, S. Wang, Y. Q. Liu, G. Z. Hao, Z. X. Wang, X. M. Song, and A. K. Wang, Phys. Plasmas **22**, 090705 (2015).
[35]E. Hameiri and S. T. Chun, Phys. Rev. A **41**, 1186 (1990).
[36]J. W. Connor, C. J. Ham, R. J. Hastie, and Y. Q. Liu, Plasma Phys. Controlled Fusion **57**, 065001 (2015).
[37]X. Bai, Y. Q. Liu, Z. Gao, G. L. Xia, and S. X. Yang, Phys. Plasmas **25**, 090701 (2018).
[38]A. H. Glasser, J. M. Greene, and J. L. Johnson, Phys. Fluids **18**, 875 (1975).
[39]Y. Q. Liu, A. Bondeson, M. S. Chu, J.-Y. Favez, Y. Gribov, M. Gryaznevich, T. C. Hender, D. F. Howell, R. J. La Haye, J. B. Lister, P. de Vries, and EFDA JET Contributors, Nucl. Fusion **45**, 1131 (2005).
[40]Y. Q. Liu, S. M. Yang, J. S. Kang, J. Van Blarcum, M. J. Choi, H. Frerichs, and S. K. Kim, Nucl. Fusion **64**, 056005 (2024).
[41]C. Wahlberg and A. Bondeson, J. Plasma Phys. **57**, 327 (1997).
[42]G. Z. Hao, Y. Q. Liu, A. K. Wang, Y. Sun, Y. H. Xu, H. D. He, M. Xu, H. P. Qu, X. D. Peng, J. Q. Xu, S. Y. Cui, and X. M. Qiu, Phys. Plasmas **21**, 122503 (2014).
[43]X. Bai, Y. Q. Liu, and G. Z. Hao, Nucl. Fusion **61**, 066016 (2021).
[44]P. Zhu, D. D. Schnack, F. Ebrahimi, E. G. Zweibel, M. Suzuki, C. C. Hegna, and C. R. Sovinec, Phys. Rev. Lett. **101**, 085005 (2008).
[45]I. T. Chapman, S. Brown, R. Kemp, and N. R. Walkden, Nucl. Fusion **52**, 042005 (2012).
[46]A. J. Webster and C. G. Gimblett, Phys. Rev. Lett. **102**, 035003 (2009).
[47]Y. Q. Liu, M. S. Chu, I. T. Chapman, and T. C. Hender, Phys. Plasmas **15**, 112503 (2008).